Manipulating elastic waves through piezoelectric metamaterial with nonlinear electrical switched Dual-connected topologies

Bin Bao, Mickaël Lallart, Daniel Guyomar

Version of Record: https://www.sciencedirect.com/science/article/pii/S0020740319347137
Manuscript_0d70d147099350e4c4970290546da469

Manipulating Elastic Waves Through Piezoelectric Metamaterial With Nonlinear Electrical Switched Dual-connected Topologies

Bin Bao[a,b*], Mickaël Lallart[a] and Daniel Guyomar[a]

[a]Univ. Lyon, INSA-Lyon, LGEF EA682,F-69621 Villeurbanne, France

[b]Department of Mechanics and Aerospace Engineering, Southern University of Science and Technology, Shenzhen 518055, China

[*]baob@sustech.edu.cn

Abstract

This research proposes a new kind of piezoelectric metamaterials with nonlinear SSDI (Synchronized Switching Damping on Inductor) Dual-connected electronic networks, which provides a new electrical medium coupled with the piezoelectric beam metamaterial for elastic wave manipulation and vibration control. Specifically, the proposed topology considers several piezoelectric elements periodically and evenly bonded onto the substructure. The proposed structure is composed of several electromechanical (EM) periodic cells. All the piezoelectric elements in one EM periodic cell are connected to each other in a cyclic fashion by identical SSDI shunts, and there is no electrical connection between every two EM periodic cells, shaping the Dual-connected electrical connection. Based on the wave propagation theory and finite element modeling, band structure and eigenmode shapes of the proposed structure are investigated for elastic wave manipulation and low-frequency vibration control. Results show that the proposed structure with SSDI 2-order-Dual-connected electrical networks exhibits broad phononic band gaps. Especially, band gap hybridization with Bragg-type band gap generation mechanism in the proposed structure with SSDI 2-order-Dual-connected electrical networks outperforms that of the piezoelectric metamaterial with SSDI independent networks. Furthermore, the low frequency vibration reduction and wave attenuation performance of the proposed structure is experimentally validated by measuring the harmonic response of a periodic clamped-clamped piezoelectric beam structure.

Keywords: vibration control; mechanical wave propagation; metamaterial; phononic; synchronized switching damping; piezoelectric; nonlinear treatment.

Nomenclature

ω angular frequency

C_0 inherent capacitance of one PZT

C_{equ} equivalent capacitance of two PZTs in series

V_{md} voltage difference between two PZTs after the inversion process

V_{Md} voltage difference between two PZTs before the inversion process

γ_{diff} $=V_{md}/V_{Md}$ denotes the inversion coefficient of the switch connected between two PZTs

V_m absolute piezoelectric voltage of one PZT after the inversion process

V_M absolute piezoelectric voltage of one PZT before the inversion process

γ $=V_m/V_M$ denotes the inversion coefficient of the switch connected to one PZT

$[M_{unit}]$ dynamic mass matrix

$[C_{unit}]$ Rayleigh damping matrix

$[K_{unit}]$ short-circuit stiffness matrix

$[H]$ matrix of Hermitian shape function

$[H'']$ matrix of second order derivative of Hermitian shape function

ρ mass density of the material

A cross-sectional area of the beam

E elastic modulus of the beam

I second moment of area of the beam structure's cross-section

β_1, β_2 Rayleigh damping coefficients

$\{d^i\}$ generalized nodal displacement vectors (displacement and slope vectors in the frequency domain)

$\{P^i\}$ generalized nodal force vectors (force and moment vectors in the frequency domain)

$\{V_p^i\}, \{I_p^i\}$ piezoelectric voltages and output currents of two identical PZTs

d_{31} piezoelectric charge constant

ε_{33}^T electrical permittivity under constant stress

s_{ij}^E $(s_{11}^E,\ s_{12}^E)$ elastic constant under constant electric field

w_b width of the beam substrate

t_b thickness of the beam substrate

t_p thickness of a single PZT

L_p length of a single PZT

u_3 displacement along the 3-axis

x_c neutral axis position

$p_1,\ p_2$ signs of piezoelectric constant depending on the polarization direction of the two PZTs within one Dual-connected cell

Z_{equ} equivalent load of the nonlinear SSDI interface

$V_{p1,\,p2}$ output voltages of piezoelectric patches 1, 2

$I_{p1,\,p2}$ output currents of piezoelectric patches 1, 2

I_m current through the load Z_{equ}

1. Introduction

Thanks to the development of periodic structures and smart materials, smart metamaterials which can generate band gaps, within which mechanical waves cannot propagate or are greatly attenuated, have attracted great attention in recent years. Traditionally, purely mechanical metamaterials [1] can generate Bragg-type stop bands for mechanical wave control. Their central frequencies are determined by the Bragg condition [2]. According to the latter, the lattice constant must be of the same order as the relevant wavelength. Therefore, low-frequency Bragg-type band gaps cannot appear in small-scale mechanical metamaterials, but only in structures featuring large dimensions, which is a limiting factor in many practical applications. By comparison, purely mechanical metamaterials based on locally resonant band gap mechanism [3] can address this limitation and generate low-frequency band gaps even in small dimensions. However, except some scalable mechanical metamaterials [4], such as morphing metamaterials using origami techniques [5], which tune mechanical properties of wave-guide meta-structures through changing their structure shape using purely geometric considerations, wave attenuation properties for most of purely mechanical metamaterials cannot be easily changed after assembly [6]. By comparison, smart metamaterials [7-10] can exhibit different resonant-type stop band characteristics by altering the resonant features in the electrical domain without changing the metamaterial shapes, since resonant-type stop bands in smart metamaterials are partially determined by the electromechanical periodicity of smart materials coupled with external electrical resonant circuits.

In this research, smart metamaterials specifically refer to piezoelectric metamaterials [11-13]. After the mechanical structure of piezoelectric metamaterial is molded and formed, mechanical structure optimization cannot be performed. Under such condition, only different electrical impedance and electrical circuit networks can be selected for optimizing the electrical medium of the piezoelectric metamaterial. Therefore, so as to improve the wave propagation performance of piezoelectric metamaterials from the electrical medium aspect, it is necessary to develop different electrical circuit networks for coupling the piezoelectric metamaterials and study the band structure and vibration transmittance properties of the piezoelectric metamaterials. In recent decades, a number of researchers have studied piezoelectric metamaterials with resonant linear electrical networks (including negative capacitance electrical networks). However, few studies have been conducted on the band structure and electromechanical coupling properties between the non-independent electric

networks and the mechanical structure of piezoelectric metamaterials, especially piezoelectric metamaterial with nonlinear electrical networks.

Specifically, for piezoelectric metamaterials with resonant linear electrical networks [14-18], Thorp *et al.* [19] adopted monomodal resonant oscillators in a piezoelectric rod metamaterial for elastic wave attenuation and localization. Locally resonant-type stop bands are generated and centered at the tuning frequencies of the electrical unimodal resonant shunt. Nevertheless, using passive shunting is limited either by the performance and robustness with respect to frequency drifts, and/or by the volume of passive components (*i.e.*, inductance) that require to be finely tuned. Furthermore, in the low frequency region, the value of the optimal inductance may be prohibitive and even unrealistic, necessitating the use of synthetic inductors that require external energy. For piezoelectric metamaterials featuring negative capacitance electrical networks [20-24], Tateo *et al*. [24] proposed a piezoelectric meta-composite plate with independent negative capacitance electrical networks for broadband vibration reduction over tunable frequency ranges. The results showed that the investigated approach provides a robust and effective vibration control solution for complex structures. However, negative capacitance shunts require the use of active electronic circuits that may consume too much energy for the targeted application.

In recent years, nonlinear elastic wave metamaterials [25-27] have exhibited promising potentials for elastic wave manipulation. In order to address the issues of energy consumption and size of electronic components, nonlinear electrical damping techniques have been introduced into piezoelectric metamaterials in the last four years. Lallart *et al.* [28] proposed a piezoelectric beam metamaterial with nonlinear electrical networks using independent SSDI (Synchronized Switching Damping on Inductor) shunts. In the investigated periodic cell, each SSDI shunt, which has self-powered versions for implementation [29], is separately connected to each PZT. Results showed that the piezoelectric metamaterial with independent SSDI electrical networks achieved much better wave attenuation performance than the piezoelectric metamaterial with pure resistor electrical networks. Broadly resonant-type band gaps can be generated by the proposed meta-structure, especially suitable for low-frequency multimodal vibration control applications. Following this concept, Yan *et al.* [30] and Bao *et al.* [31-33] then proposed several different piezoelectric metamaterial systems with nonlinear electrical networks in which electrical irregularities and nonlinearities are introduced into the electromechanical metamaterial design for enhancing wave attenuation and vibration reduction performance in some specific frequency bands, especially in the low frequency region.

However, such piezoelectric metamaterials combined with nonlinear electrical networks for elastic wave manipulation are still rarely reported in recent years.

In order to further investigate EM coupling mechanism between the mechanical medium and the electrical medium including nonlinear SSDI shunts for wave propagation and vibration control, this article proposes a new piezoelectric metamaterial with nonlinear SSDI Dual-connected electrical networks for optimizing and controlling the elastic wave properties of the piezoelectric metamaterial. Specifically, the proposed structure includes N piezoelectric elements periodically and evenly spaced attached on the beam structure. And it is composed of N_g (N_g=*2, 3, 4…*) EM (electromechanical) periodic cells. Every EM periodic cell includes N (N=*2, 3, 4…*) Bragg-type periodic cells. Each Bragg-type periodic cell includes only one piezoelectric element. Thus the proposed beam structure includes N_b (N_b=N_g×N, N_g=*2, 3, 4…*, N=*2, 3, 4…*) Bragg-type periodic cells. In the EM periodic cell, every two adjacent piezoelectric elements are connected each other by an identical SSDI shunt, and the piezoelectric elements at the both ends of the EM periodic cell are also connected by identical SSDI shunt. Thus, all the piezoelectric elements are connected in a circle by identical SSDI shunts in one EM periodic cell. In addition, there is no electrical connection between every two adjacent EM periodic cells. Band structure and vibration transmittance of the proposed structure are investigated for elastic wave manipulation and low-frequency vibration control based on the wave propagation theory and finite element modeling. The article is organized as follows. Section 2 introduces the basic principle of nonlinear SSDI technique and SSDI impedance estimation. In Section 3, the wave and finite element modeling approach for predicting the propagative wave within the proposed electromechanical metamaterial is presented. Section 4 aims at analyzing mechanical wave propagation characteristics of the proposed structure. In Section 5, the low-frequency structural damping performance of the proposed structure is experimentally validated and discussed. Conclusions on the presented work are eventually given in Section 6.

2. Basics of nonlinear SSDI (Synchronized Switch Damping on Inductor) technique

The principles of the nonlinear Synchronized Switch Damping on Inductor (SSDI) technique consist of quickly inverting the piezoelectric voltage on each displacement extremum of the structure, which yields a voltage magnification through a cumulative process as well as a decrease of the time shift between voltage and velocity. Such voltage inversion and shift processes therefore denote an increase of the mechanical

energy irreversibly converted into electrical energy, thus significantly reducing the mechanical energy within the structure. Specifically, in this research, as shown in Figure 1(a), a SSDI control shunt, composed of an electronic switch in series with an inductor, is applied between two identical PZTs bonded on the piezoelectric structure, which is represented schematically in Figure 1(b). When the PZT is in open-circuit condition, the piezoelectric voltage varies with the piezoelectric strain difference in a linear fashion. When an extremal voltage difference between two PZTs appears, the switch is closed, and an oscillator, composed of the inductance L and the equivalent inherent capacitance of the two PZTs, is formed. The switching time period is equal to half of the pseudo-period of this oscillator. For most of the time in one mechanical vibration period, the switch is open.

The technique is adaptive to frequency shifts due to the extremum detection principles. Precisely, according to the literatures [32], the nonlinear SSDI impedance Z of the SSDI control shunt connected between two identical PZTs, and the SSDI impedance Z_{ind} of the SSDI control shunt independently connected to one PZT can be estimated by using first harmonic approximation in the frequency domain, yielding：

$$\begin{cases} Z = \dfrac{\pi\left(1-\gamma_{diff}\right)}{4\omega C_{equ}\left(1+\gamma_{diff}\right)} + j\dfrac{1}{\omega C_{equ}}, C_{equ} = \dfrac{C_0}{2} \\ Z_{ind} = \dfrac{\pi\left(1-\gamma\right)}{4\omega C_0\left(1+\gamma\right)} + j\dfrac{1}{\omega C_0}, \gamma_{diff} = \gamma^{\sqrt{\frac{1}{2}}} \end{cases} \tag{1}$$

As described by above equations, the imaginary terms of the nonlinear SSDI impedances are the optimized imaginary parts of the electronic load in the independent and Dual-connected methods, which means that the SSDI shunt has the capability of automatic impedance adaptation. In addition, the inversion coefficient γ_{diff} in the interconnected method is greater than γ since the equivalent piezoelectric capacitance in the Dual-connected topology is less than that in the independent method. The stability of control system is important for elastic wave metamaterial [34]. The SSDI control system has high system stability, which is validated by the reference [32].

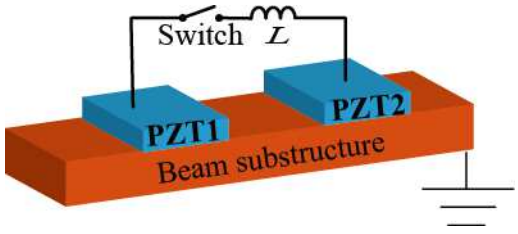

(a)

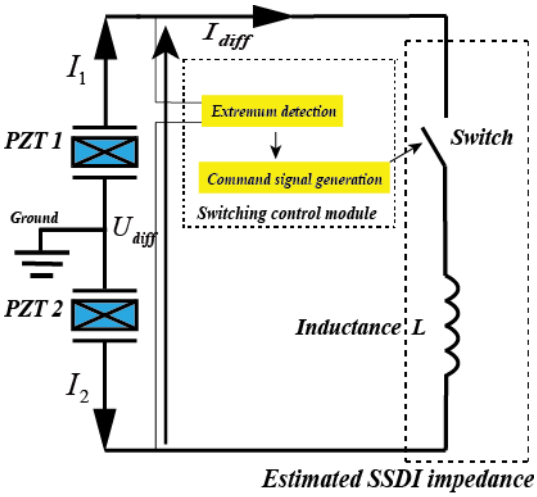

(b)

Figure 1 (a) SSDI shunt connected between two identical PZTs of the structure; (b) schematic diagram of the differential SSDI control device.

3. Modeling for the proposed beam metamaterial using SSDI Dual-connected electrical networks

3.1 Overview of the proposed structure

As shown in Figure 2(a), there are N_b (N_b=N_g×N, N_g=2, 3, 4…, N=2, 3, 4…) identical piezoelectric elements periodically and evenly spaced attached to the beam substructure in the proposed beam metamaterial with SSDI Dual-connected electronic networks. It is composed of N_g EM periodic cells. In the EM periodic cell of the proposed structure as shown in Figure 2(b), there are N Bragg-type periodic cells connected each other by the same SSDI shunt. Two Bragg-type periodic cells at both ends of the EM periodic cell are also connected by the SSDI shunt. There is no electrical connection between every two adjacent EM periodic cells which form the Dual-connected electrical connection. Each Bragg-type periodic cell include only one piezoelectric element. Herein, N not only denotes the number of Bragg-type periodic cells composing a minimal N-order EM periodic cell, but also the order of the Dual-connected electronic networks. The estimated impedance of the SSDI shunt between two PZTs is equal to Z.

Physically, the EM periodic cell of proposed structure is comprised of two coupling media: electrical one and mechanical one. The mechanical medium includes several identical PZTs periodically placed throughout the beam substrate, while the electrical medium denotes the SSDI Dual-connected electrical networks coupled with the

electrical characteristics of the PZTs. Bragg-type band gap generation mechanism depends on the mechanical medium, and resonance-type band gap generation mechanism is mainly linked to the electrical medium. As shown in Figure 2, I_{M1}, …I_{Mi}, …I_{MN} ($i \in [2,3,4,5,\ldots N]$) respectively denotes the currents flowing through the N SSDI shunt branches among piezoelectric elements. I_1, …I_i, …I_N ($i \in [2,3,4,5,\ldots N]$) respectively refers to the the output currents from the piezoelectric elements of the EM periodic cell. Finally, V_1, …V_i, …V_N ($i \in [2,3,4,5,\ldots N]$) are the respective output voltages of the piezoelectric elements in the EM periodic cell.

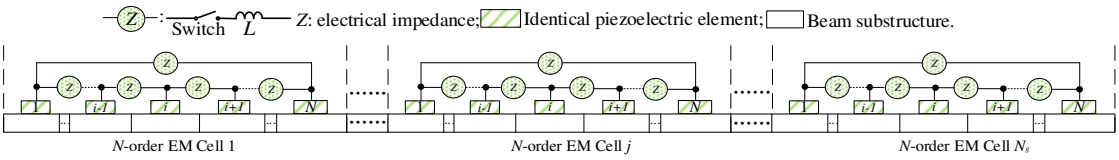

(a)

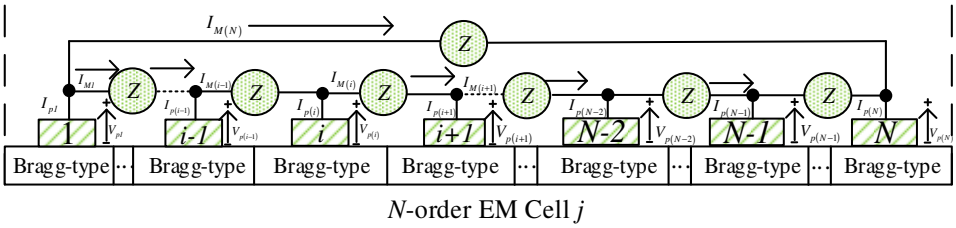

(b)

Figure 2 (a) Proposed piezoelectric metamaterial with SSDI N-order Dual-connected electronic networks; (b) one N-order EM cell of the proposed structure.

In order to clearly exhibit the wave propagation properties and the schematics of the proposed structure with SSDI N-order Dual-connected electronic networks, the SSDI 2-order Dual-connected electronic networks and the SSDI 3-order Dual-connected electronic networks for coupling the piezoelectric metamaterials are given and investigated as shown in Figure 3 and Figure 4. In one 2-order Dual-connected periodic cell of the proposed structure, two PZTs in every two adjacent minimal Bragg-type periodic cells are connected by the SSDI shunt. While in one 3-order Dual-connected periodic cell of the proposed structure, three PZTs in every three adjacent minimal Bragg-type periodic cells are connected each other by the SSDI shunt.

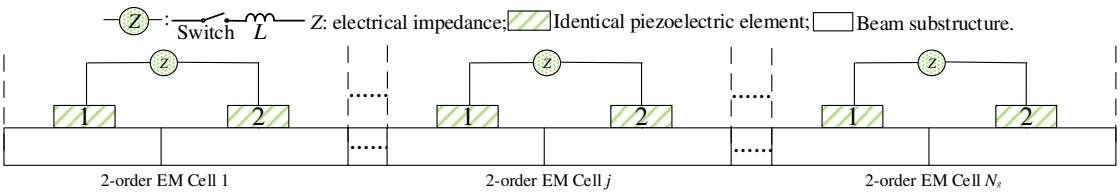

(a)

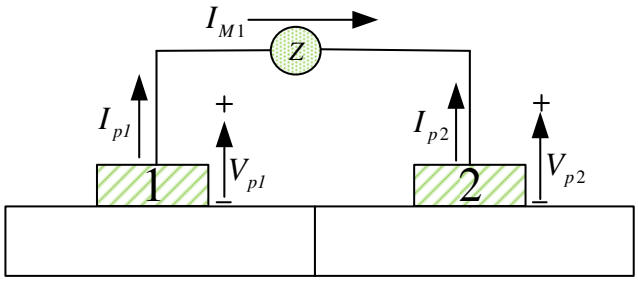

2-order EM Cell *j*

(b)

Figure 3 (a) Proposed piezoelectric metamaterial with nonlinear SSDI 2-order Dual-connected electronic networks; (b) one 2-order EM cell of the proposed structure with SSDI *2*-order Dual-connected electronic networks.

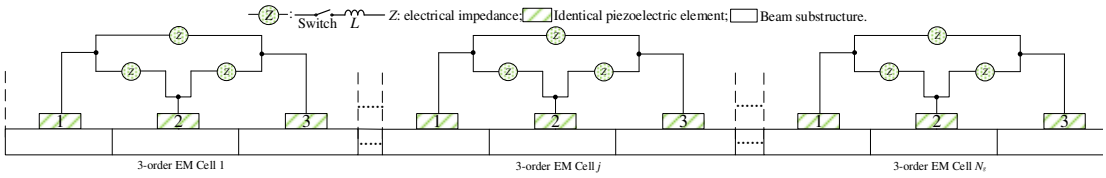

(a)

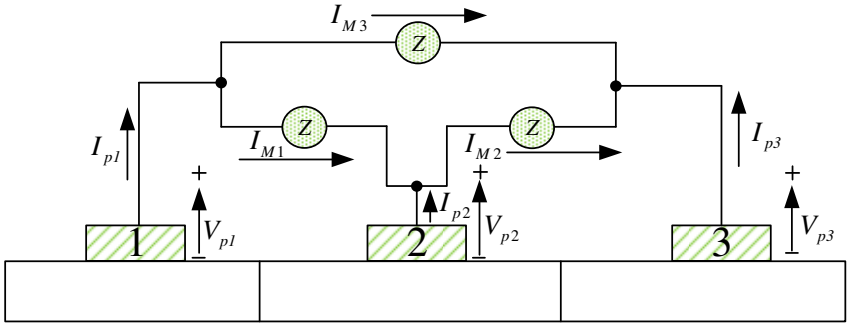

3-order EM Cell *j*

(b)

Figure 4 (a) Proposed piezoelectric metamaterial with nonlinear SSDI 3-order Dual-connected electronic networks; (b) one 3-order EM cell of the proposed structure with SSDI 3-order Dual-connected electronic networks.

3.2 Modeling of the proposed structure with SSDI N-order Dual-connected electronic networks.

According to the FEM (finite element modeling) method of an Euler-Bernoulli piezoelectric beam [35], assuming the proposed beam structure fits Euler-Bernoulli beam hypotheses, and considering that the *N*-order Dual-connected periodic cell in the

proposed metamaterial can be divided into n finite elements, the fundamental EM relationships in the frequency domain within a N-order Dual-connected periodic cell can be given by:

$$\begin{cases} \left[-\omega^2 M_{cell}\right]\left\{d^{ni}\right\}+\left[j\omega C_{cell}\right]\left\{d^{ni}\right\}+\left[K_{cell}\right]\left\{d^{ni}\right\}+\left[B_1^{N-order}\right]\left\{V_p\right\}=\left\{P^{ni}\right\} \\ \left\{I_p\right\}=\left[j\omega B_2^{N-order}\right]\left\{d^{ni}\right\}+\left[j\omega B_3^{N-order}\right]\left\{V_p\right\} \end{cases} \tag{2}$$

$$[M_{cell}]=\int_0^l [H]^T \rho A [H] dx, \quad [K_{cell}]=\int_0^l [H'']^T EI [H''] dx, \quad [C_{cell}]=\beta_1 [M_{cell}]+\beta_2 [K_{cell}]$$

where M_{cell}, C_{cell}, K_{cell} respectively denote the matrices of the mass, Rayleigh damping and short-circuit stiffness. l is the length of finite beam element. H and H'' respectively denote the matrix of Hermitian shape function and the second order derivative of Hermitian shape functions. ρ denotes the mass density of the material, A denotes the cross-sectional area of the beam, E the elastic modulus of the beam, and I denotes the second moment of the cross-sectional area of the beam. β_1 and β_2 are the damping coefficient constants. d^{ni} and P^{ni} (2(n+1) by 1 matrices) respectively denote the generalized nodal displacement vectors (displacement and slope vectors in the frequency domain) and the generalized nodal force vectors (force and moment vectors in the frequency domain). $\{V_p\}$ and $\{I_p\}$ are the piezoelectric voltages and output currents of identical piezoelectric elements in the investigated periodic cell, and their matrix size is determined by the number of piezoelectric elements in the unit investigated EM periodic cell. Detailed derivation of Eq. (2) is shown in the appendix.

$$I_p=\begin{bmatrix} I_{p1} \\ \cdots \\ I_{pi} \\ \cdots \\ I_{pN} \end{bmatrix}, V_p=\begin{bmatrix} V_{p1} \\ \cdots \\ V_{pi} \\ \cdots \\ V_{pN} \end{bmatrix} \tag{3}$$

$B_1^{N\text{-order}}$ and $B_2^{N\text{-order}}$ are a $2(n+1)$ by N and a N by $2(n+1)$ EM matrices given by:

$$B_1^{N\text{-order}}=\left[B_{11} \quad \cdots \quad B_{1i} \quad \cdots \quad B_{1N}\right], \begin{cases} B_{11}=b_{11}\int_0^l [H'']^T dx, b_{11}=-\dfrac{p_1 d_{31} w_b}{t_p\left(s_{11}^E+s_{12}^E\right)}\displaystyle\int_{t_b}^{t_b+t_p}\left(u_3-x_c\right)dx_3 \\ \cdots \\ B_{1i}=b_{1i}\int_0^l [H'']^T dx, b_{1i}=-\dfrac{p_i d_{31} w_b}{t_p\left(s_{11}^E+s_{12}^E\right)}\displaystyle\int_{t_b}^{t_b+t_p}\left(u_3-x_c\right)dx_3 \\ \cdots \\ B_{1N}=b_{1N}\int_0^l [H'']^T dx, b_{1N}=-\dfrac{p_N d_{31} w_b}{t_p\left(s_{11}^E+s_{12}^E\right)}\displaystyle\int_{t_b}^{t_b+t_p}\left(u_3-x_c\right)dx_3 \end{cases} \tag{4}$$

$$B_2^{N-order}=\begin{bmatrix}B_{21}\\ \dots\\ B_{2i}\\ \dots\\ B_{2N}\end{bmatrix},\begin{cases}B_{21}=b_{21}\int_0^l[H'']dx,\ b_{21}=-\dfrac{p_1d_{31}t_p}{\left(s_{11}^E+s_{12}^E\right)}\\ \dots\\ B_{2i}=b_{2i}\int_0^l[H'']dx,\ b_{2i}=-\dfrac{p_id_{31}t_p}{\left(s_{11}^E+s_{12}^E\right)}\\ \dots\\ B_{2N}=b_{2N}\int_0^l[H'']dx,\ b_{2N}=-\dfrac{p_Nd_{31}t_p}{\left(s_{11}^E+s_{12}^E\right)}\end{cases} \tag{5}$$

$B_3^{N\text{-}order}$ is a *2* by *2* electrical (capacitance) matrix whose expression yields:

$$B_3^{N-order}=\begin{bmatrix}B_{31} & \dots & 0 & \dots & 0\\ \dots & \dots & \dots & \dots & \dots\\ 0 & \dots & B_{3i} & \dots & 0\\ \dots & \dots & \dots & \dots & \dots\\ 0 & \dots & 0 & \dots & B_{3N}\end{bmatrix},\ B_{31}=B_{3i}=B_{3N}=\frac{w_bL_p\left[2d_{31}{}^2-\varepsilon_{33}^T\left(s_{11}^E+s_{12}^E\right)\right]}{t_p\left(s_{11}^E+s_{12}^E\right)} \tag{6}$$

The N-order Dual-connected periodic cell (Figure 2) therefore holds the following relationships:

$$\begin{bmatrix}1 & -1 & 0 & 0 & 0 & 0 & 0 & 0 & -Z & 0 & 0 & 0\\ \dots & \dots & \dots & \dots & \dots & \dots & \dots & \dots & \dots & \dots & \dots & \dots\\ 0 & 0 & 1 & -1 & 0 & 0 & 0 & 0 & 0 & 0 & -Z & 0\\ 1 & 0 & 0 & -1 & 0 & 0 & 0 & 0 & 0 & 0 & 0 & -Z\\ -j\omega B_{31} & 0 & 0 & 0 & 1 & 0 & 0 & 0 & 0 & 0 & 0 & 0\\ \dots & -j\omega B_{32} & \dots & \dots & \dots & \dots & \dots & \dots & \dots & \dots & \dots & \dots\\ 0 & 0 & -j\omega B_{3(N-1)} & 0 & 0 & 0 & 1 & 0 & 0 & 0 & 0 & 0\\ 0 & 0 & 0 & -j\omega B_{3N} & 0 & 0 & 0 & 1 & 0 & 0 & 0 & 0\\ 0 & 0 & 0 & 0 & -1 & 0 & 0 & 0 & 1 & 0 & 0 & 1\\ \dots & \dots & \dots & \dots & \dots & \dots & \dots & \dots & \dots & \dots & \dots & \dots\\ 0 & 0 & 0 & 0 & 0 & 0 & -1 & 0 & 0 & -1 & 1 & 0\\ 0 & 0 & 0 & 0 & 0 & 0 & 0 & 1 & 0 & 0 & 1 & 1\end{bmatrix}\cdot\begin{bmatrix}V_{p1}\\ V_{pi}\\ V_{p(N-1)}\\ V_{pN}\\ I_{p1}\\ I_{pi}\\ I_{p(N-1)}\\ I_{pN}\\ I_{M1}\\ I_M\\ I_{M(N-1)}\\ I_{MN}\end{bmatrix}+\begin{bmatrix}0\\ 0\\ 0\\ 0\\ -j\omega B_{21}\\ -j\omega B_{2i}\\ -j\omega B_{2(N-1)}\\ -j\omega B_{2N}\\ 0\\ 0\\ 0\\ 0\end{bmatrix}d^{ni}=0 \tag{7}$$

According to the above electrical relationships, the expressions linking the generalized nodal displacement vectors d^{ni} and the output voltages V_p of the PZTs in one EM periodic cell can be obtained. For instance, the 2-order Dual-connected periodic cell (Figure 3) has the following relationships:

$$\begin{bmatrix}1 & -1 & -Z & 0\\ -1 & 1 & 0 & -Z\\ -j\omega B_{31} & 0 & 1 & 0\\ 0 & -j\omega B_{32} & 0 & 1\end{bmatrix}\begin{bmatrix}V_{p1}\\ V_{p2}\\ I_{p1}\\ I_{p2}\end{bmatrix}+\begin{bmatrix}0\\ 0\\ -j\omega B_{21}\\ -j\omega B_{22}\end{bmatrix}d^{ni}=0 \tag{8}$$

Therefore, $V_p^{2\text{-}order}$ can be obtained as:

$$V_p^{2\text{-}order}=\begin{bmatrix}V_{p1}\\V_{p2}\end{bmatrix}=B_6^{2-order}d^{ni},\ B_6^{2-order}=\begin{bmatrix}B_{61}^{2-order}\\B_{62}^{2-order}\end{bmatrix} \tag{9}$$

$$V_{p1}=\left[\frac{-\left(\frac{B_{21}+B_{22}}{B_{31}}\right)+j\omega ZB_{21}}{2-j\omega ZB_{31}}\right]d^{ni}=B_{61}^{2-order}d^{ni} \tag{10}$$

$$V_{p2}=\left[-\left(\frac{B_{21}+B_{22}}{B_{31}}\right)-\frac{-\left(\frac{B_{21}+B_{22}}{B_{31}}\right)+j\omega ZB_{21}}{2-j\omega ZB_{31}}\right]d^{ni}=B_{62}^{2-order}d^{ni} \tag{11}$$

Similarly, the 3-order Dual-connected periodic cell (Figure 4) has the following relationships:

$$\begin{bmatrix}1&-1&0&0&0&0&-Z&0&0\\0&1&-1&0&0&0&0&-Z&0\\1&0&-1&0&0&0&0&0&-Z\\-j\omega B_{31}&0&0&1&0&0&0&0&0\\0&-j\omega B_{32}&0&0&1&0&0&0&0\\0&0&-j\omega B_{33}&0&0&1&0&0&0\\0&0&0&-1&0&0&1&0&1\\0&0&0&0&-1&0&-1&1&0\\0&0&0&0&0&1&0&1&1\end{bmatrix}\cdot\begin{bmatrix}V_{p1}\\V_{p2}\\V_{p3}\\I_{p1}\\I_{p2}\\I_{p3}\\I_{M1}\\I_{M2}\\I_{M3}\end{bmatrix}+\begin{bmatrix}0\\0\\0\\-j\omega B_{21}\\-j\omega B_{22}\\-j\omega B_{23}\\0\\0\\0\end{bmatrix}d^{ni}=0 \tag{12}$$

And then, $V_p^{3\text{-}order}$ can be obtained as:

$$V_p^{3\text{-}order}=\begin{bmatrix}V_{p1}\\V_{p2}\\V_{p3}\end{bmatrix}=B_6^{3-order}d^{ni},\ \ B_6^{3-order}=\begin{bmatrix}B_{61}^{3-order}\\B_{62}^{3-order}\\B_{63}^{3-order}\end{bmatrix} \tag{13}$$

$$V_{p1}=\left[\frac{-jZ^2\omega^2B_{21}B_{31}^2+Z\omega B_{31}\left(4B_{21}+B_{22}+B_{23}\right)+3j\left(B_{21}+B_{22}+B_{23}\right)}{B_{31}\left(Z\omega B_{31}+3j\right)\left(jZ\omega B_{31}-3\right)}\right]d^{ni}=B_{61}^{3-order}d^{ni} \tag{14}$$

$$V_{p2}=\left[\frac{-jZ^2\omega^2B_{22}B_{31}^2+Z\omega B_{31}\left(B_{21}+4B_{22}+B_{23}\right)+3j\left(B_{21}+B_{22}+B_{23}\right)}{B_{31}\left(Z\omega B_{31}+3j\right)\left(jZ\omega B_{31}-3\right)}\right]d^{ni}=B_{62}^{3-order}d^{ni} \tag{15}$$

$$V_{p3}=\left[\frac{-jZ^2\omega^2B_{23}B_{31}^2+Z\omega B_{31}\left(B_{21}+B_{22}+4B_{23}\right)+3j\left(B_{21}+B_{22}+B_{23}\right)}{B_{31}\left(Z\omega B_{31}+3j\right)\left(jZ\omega B_{31}-3\right)}\right]d^{ni}=B_{63}^{3-order}d^{ni} \tag{16}$$

Denoting the dynamical stiffness matrix of the short-circuited system $[A_{cell}]$, that is therefore equal to $\left[-\omega^2M_{cell}\right]+\left[j\omega C_{cell}\right]+\left[K_{cell}\right]$, and the dynamical relationships of the Dual-connected EM periodic cell can yield:

$$\left\{P^{ni}\right\} = A_{Dual-connected}^{N-order} \cdot d^{ni} = \left(A_{cell} + B_1^{N-order} B_6^{N-order}\right) \cdot d^{ni} \tag{17}$$

4. Wave propagation properties of the proposed structure

4.1 Wave propagation comparison between the SSDI 2-order Dual-connected method and the SSDI 3-order Dual-connected method.

For simplifying and predicting the wave propagation analysis of the proposed structure with SSDI N-order Dual-connected electrical networks, herein, the SSDI 2-order and 3-order Dual-connected methods are investigated and their wave propagation performance are compared in the investigated frequency range based on a beam sample whose parameters are listed in Table 1 and Table 2 (the parameters corresponding to the experimental test structure used in Section 5). Figure 5 shows the investigated periodic cell with four different electrical medium methods for coupling the mechanical medium of the piezoelectric metamaterial. For fair comparison, each investigated periodic cell in different electrical medium methods includes 6 minimal Bragg-type periodic cells in this section. The dimension of a minimal Bragg-type periodic cell is 22 mm. Each piezoelectric element in the middle of the beam substructure of a minimal Bragg-type periodic cell is 10 mm long. Specifically, there is no electrical connection to Bragg-type periodic cells in the open circuit method, and 6 independent EM periodic cells are considered in the SSDI independent method. For the SSDI 2-order and 3-order Dual-connected methods, each investigated periodic cell respectively includes 3 2-order EM periodic cells and 2 3-order EM periodic cells.

Table 1 Dimensional and material properties of the beam substructure

Young modulus	$Y_b=190\times10^9 Pa$	Poisson ratio	$v_b=0.21$	Beam density	$\rho_b=7875\ kg/m^3$
Beam length	$L_b=176mm$	Beam width	$w_b=35mm$	Beam thickness	$t_b=1.5mm$

Table 2 Dimensional and material properties of the piezoelectric element

Short-circuit Compliance	$s_{11}^E=10.7\times10^{-12}m^2/N$ $s_{12}^E=-3.3\times10^{-12}m^2/N$	PZT length	$L_p=10mm$
Charge coefficient	$d_{31}=-108\times10^{-12}m/V$	PZT thickness	$t_p=0.5mm$

Relative dielectric constant	$\varepsilon^T/\varepsilon_0$=1150	PZT density	ρ_p=7650 kg/m^3

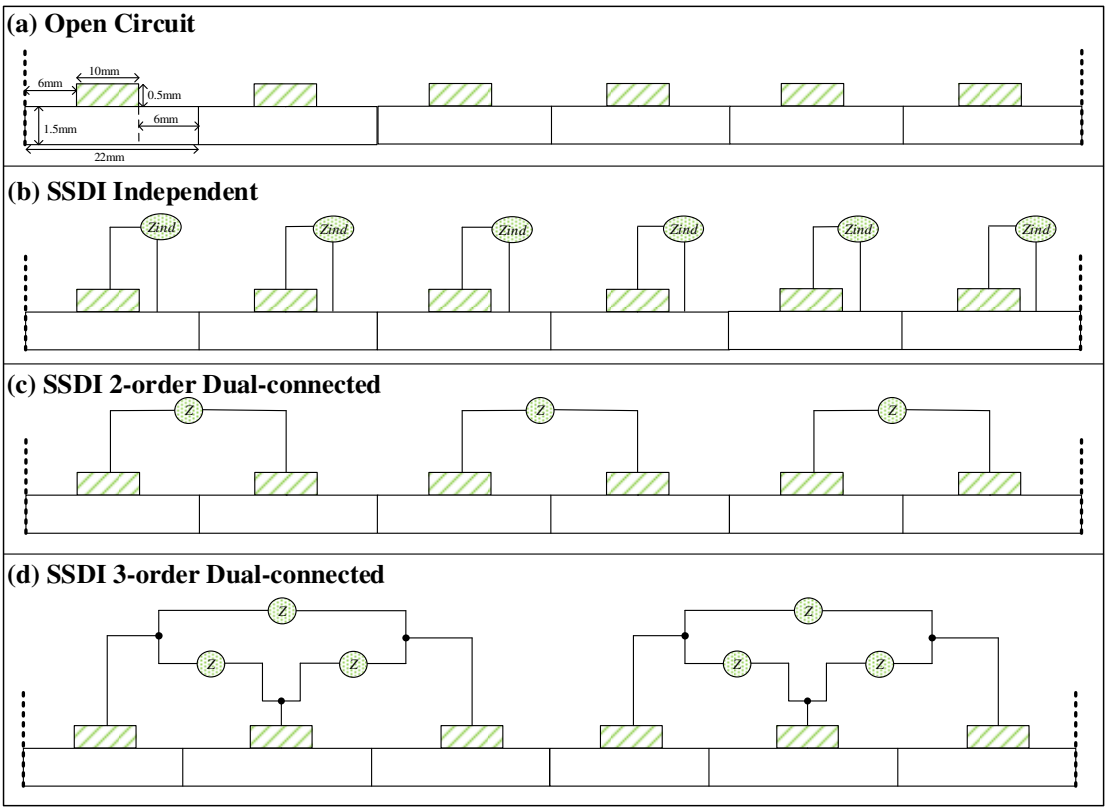

Figure 5 The investigated periodic cell (a) with no electrical connection to Bragg-type periodic cells; (b) with SSDI independent electrical networks; (c) with SSDI 2-order Dual-connected electrical networks; (d) with SSDI 3-order Dual-connected electrical networks.

According to FEM analysis, the investigated periodic cell can be decomposed into several finite elements. In order to obtain propagation coefficients (attenuation and phase) of the investigated periodic cell under different electrical media, transfer matrix for the whole cell is derived using transfer matrix method. Herein, attenuation coefficient denotes the logarithmic decay of the vibration amplitude of an elastic wave propagating from one periodic cell to the next one. Phase coefficient denotes the phase difference between the wave in two adjacent periodic cells. Only positive direction is taken into account in following analysis and no structural damping ($[\boldsymbol{C}_{cell}]$= [0]) is considered.

Figure 6 shows the attenuation and phase coefficients of propagative wave under different electrical boundary conditions. In open circuit condition, two separate Bragg-type bandgaps appear in the frequency ranges [7.2 kHz, 8.1 kHz] ∪ [29 kHz, 32 kHz]. Due to Bragg scattering, bandgaps representing frequency intervals in which

wave propagation is not allowed or attenuated, are generated at wavelengths comparable to the spatial scale of the periodicities in the periodic structures. Such bandgaps are called Bragg-type bandgaps, whose central frequencies are determined by the Bragg condition:

$$L = nn\left(\frac{\lambda}{2}\right)(nn = 1,2,3...) \tag{18}$$

Herein, L is the lattice constant of the periodic system and λ is the wavelength of elastic waves in the host material.

The SSDI independent method can achieve broad resonance bandgaps in the whole investigated frequency range, while the SSDI 2-order Dual-connected method can achieve better wave attenuation performance than the SSDI independent method in the frequency range [3.35 kHz, 13.9 kHz]. However, the wave attenuation performance of the SSDI 2-order Dual-connected method is worse than that of the SSDI independent method in other frequency domains. With the increase of the order of the Dual-connected electrical networks, it can be seen that the wave attenuation performance of the SSDI 3-order Dual-connected method is globally worse than that of the SSDI 2-order Dual-connected method. Therefore, it can be predicted that the increase of the order of the Dual-connected electrical networks will weaken the wave propagation performance of the piezoelectric metamaterial when the SSDI shunts are applied to the Dual-connected electrical networks for coupling the mechanical medium of the piezoelectric metamaterial. However, the SSDI 2-order Dual-connected networks is still worth to be further investigated for enhancing the wave attenuation performance in some specific frequency domains.

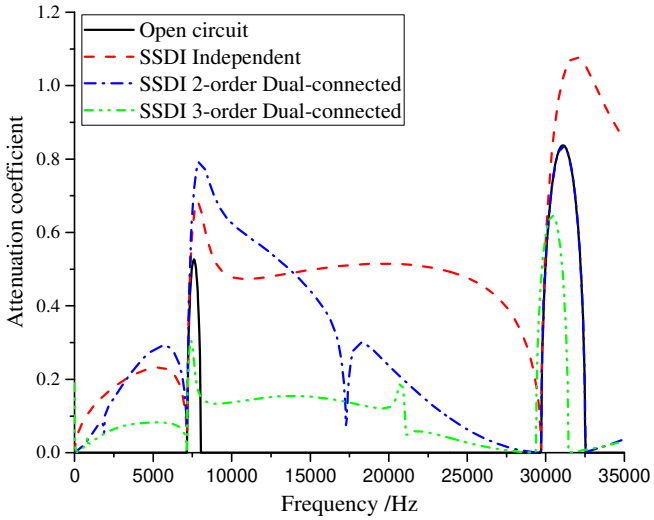

Figure 6 Attenuation coefficient curves of propagative wave in the proposed structure with different SSDI Dual-connected electrical networks (γ_{diff}=0.6) compared with the SSDI independent method (γ=0.5) and the open circuit condition, corresponding to Figure 5.

4.2 Wave propagation analysis for the proposed structure with SSDI 2-order Dual-connected electronic networks under different polarizations of the piezoelectric inserts.

In order to further investigate wave propagation properties of the SSDI 2-order Dual-connected electrical networks for coupling the mechanical medium of the piezoelectric metamaterial, the 2-order Dual-connected periodic cell is divided into two kinds: PP configuration and PN configuration that are depicted in Figure 7. Specifically, PP configuration denotes two PZTs with the same polarization direction in one Dual-connected periodic cell and PN configuration two PZTs with opposite polarization direction in one Dual-connected periodic cell. More specifically, the signs of piezoelectric constant depend on the polarization direction of the PZTs (1, 2): when the direction is positive (P), it is assumed equal to 1, and when negative (N), it is assumed equal to -1.

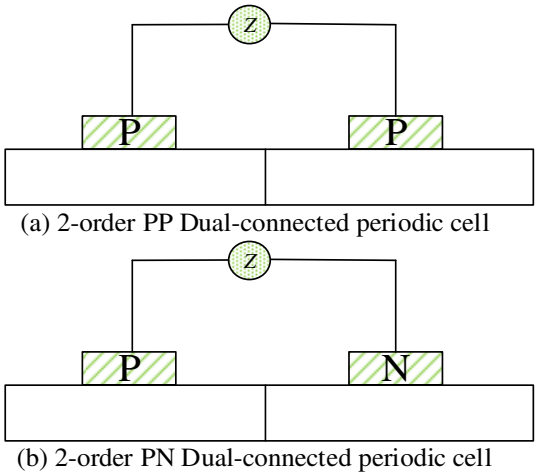

Figure 7 (a) 2-order PP Dual-connected periodic cell; (b) 2-order PN Dual-connected periodic cell.

As shown in Figure 8 for the SSDI 2-order PP/PN Dual-connected methods, the attenuation and phase coefficients of propagative wave can be obtained from the previous analysis. Similarly in the open circuit condition, two separate Bragg-type stop bands appear in the frequency ranges [7.2 kHz, 8.1 kHz]∪[29 kHz, 32 kHz]. In addition, phase coefficient of propagative wave is equal to zero within the Bragg-type band gaps in the open circuit condition, as shown in Figure 9. For fairly comparing attenuation performance of resonant-type band gaps and band gap hybridization, performance comparison is conducted between two minimal independent periodic cells with two identical SSDI shunts and one minimal PP / PN Dual-connected periodic cell with one SSDI shunt as shown in Figure 8. Results show that, compared to the SSDI independent method, the SSDI Dual-connected method exhibits better attenuation performance in the frequency range [3.35 kHz, 13.9 kHz] for SSDI PP Dual-connected method, and in the frequency ranges [0 Hz, 840 Hz]∪[21.2 kHz, 35 kHz] for SSDI PN Dual-connected method, although the enhancement is quite moderate for the latter case. Therefore, the SSDI PP / PN Dual-connected methods can use less SSDI shunts than the SSDI independent method to achieve better attenuation performance in some relatively broad frequency ranges close to Bragg-type stop bands.

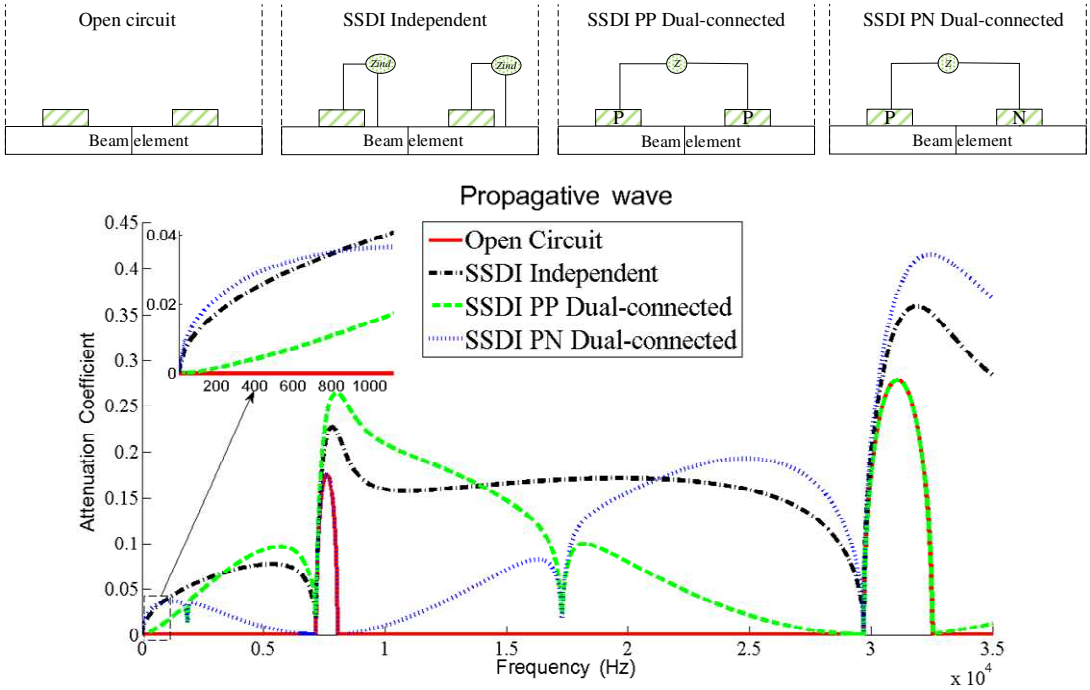

Figure 8 Attenuation coefficient curves of propagative wave in the proposed metamaterial with the SSDI PP / PN Dual-connected networks (γ=0.5, γ_{diff}=0.6).

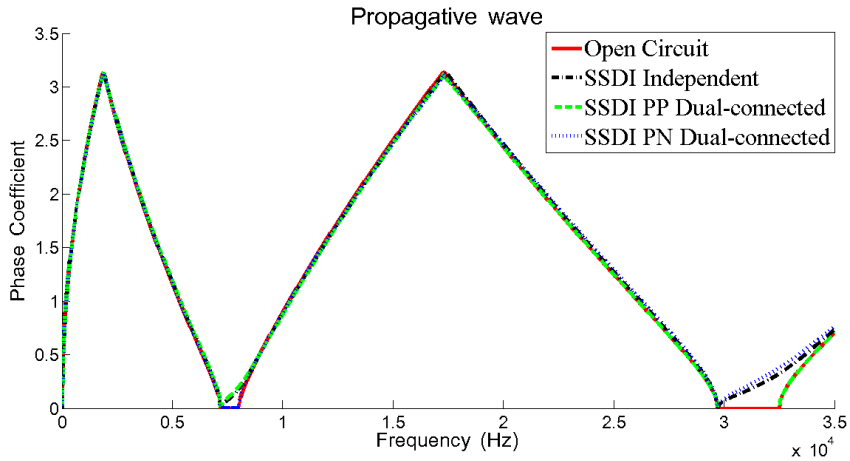

Figure 9 Phase coefficient curves of propagative wave in the proposed metamaterial with the SSDI PP / PN Dual-connected networks (γ=0.5, γ_{diff}=0.6).

Herein, the flexural vibration of beams along *x*-*z* direction is the only considered motion in beam metamaterials. In order to better demonstrate the underlying physical mechanisms of the 2-order PP/PN Dual-connected periodic cell, several eigenmode shapes (in different frequency regions) of the Dual-connected periodic cell including two identical PZTs in open circuit condition are calculated numerically by FE method based on a unit cell onto which Floquet-Bloch boundary conditions are imposed, together with the corresponding flexural vibration displacement vector fields, as

shown in Figure 10. To be specific, as shown in Figure 8, SSDI PN Dual-connected method achieves better attenuation performance than the SSDI PP Dual-connected method in the frequency range [0 Hz, 840 Hz]. For example, both of PZTs in the eigenmode shape A (167Hz) are bended and stretched as shown in Figure 10. Due to the same strain direction of two PZTs in the eigenmode shape A, the voltage difference between the two PZTs in the PN configuration is greater than that with the PP configuration, and thus PN Dual-connected periodic cell using SSDI shunt allows a much better mechanical to electrical energy conversion, and thus more electrical energy is dissipated into the switching branch.

In the frequency range [3.35 kHz, 13.9 kHz], SSDI PP Dual-connected method exhibits better attenuation performance than the SSDI PN Dual-connected method as shown in Figure 8. One of two PZTs in the Dual-connected periodic cell is bended and stretched and the other one is bended and compressed (*e.g.*, eigenmode shapes B1 (4.18kHz) and B2 (11.717kHz) as shown in Figure 10), and thus the voltage difference between two PZTs with the PP configuration is greater than that with the PN configuration because of the opposite strain direction of two PZTs in these eigenmode shapes. Hence, the SSDI PP Dual-connected method can get better attenuation performance than the SSDI PN Dual-connected method under such conditions.

In the frequency range [21.2 kHz, 35 kHz], better attenuation performance can be achieved in the SSDI PN Dual-connected method than the SSDI PP Dual-connected method as shown in Figure 8. As an example, eigenmode shapes C1 (22.385kHz) and C2 (27.789kHz), within this frequency range as shown in Figure 10, show that the two PZTs in one Dual-connected periodic cell are all bended and compressed and have the same strain direction, and thus the voltage difference in the PN configuration is higher than that in the PP configuration (as in the low frequency - [0 Hz, 840 Hz]. - region). Therefore, the SSDI PN approach can achieve better attenuation performance than the SSDI PP approach.

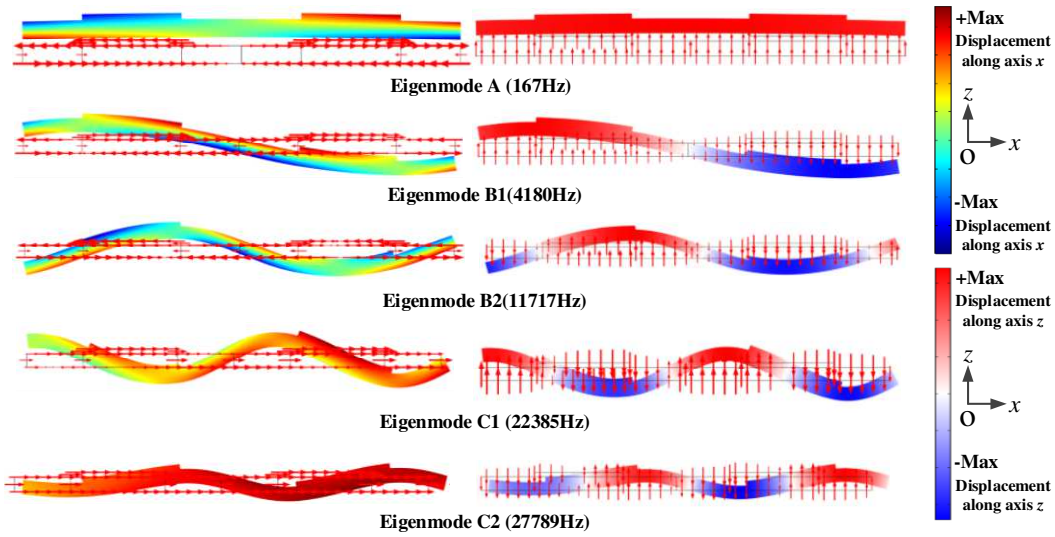

Figure 10 Eigenmode shapes in the different frequency regions, and the corresponding flexural vibration displacement vector fields (along axis x and along z) of the Dual-connected periodic cell (including two identical piezoelectric elements in the open circuit condition) represented by the color distribution and red arrows (displacement direction).

Figure 11 shows 3D plots of attenuation coefficient of propagative wave for the SSDI PP / PN Dual-connected methods versus voltage inversion coefficient compared with the SSDI independent method. With the increase of voltage inversion coefficient, all the wave attenuation performances are enhanced in different methods. Although the SSDI independent has globally better attenuation performance than the SSDI PP / PN Dual-connected methods, SSDI PP Dual-connected shows better attenuation performance close to the first Bragg-type band gap, while the SSDI PN Dual-connected method exhibits better attenuation performance below 1.5 kHz and near the second Bragg-type band gap.

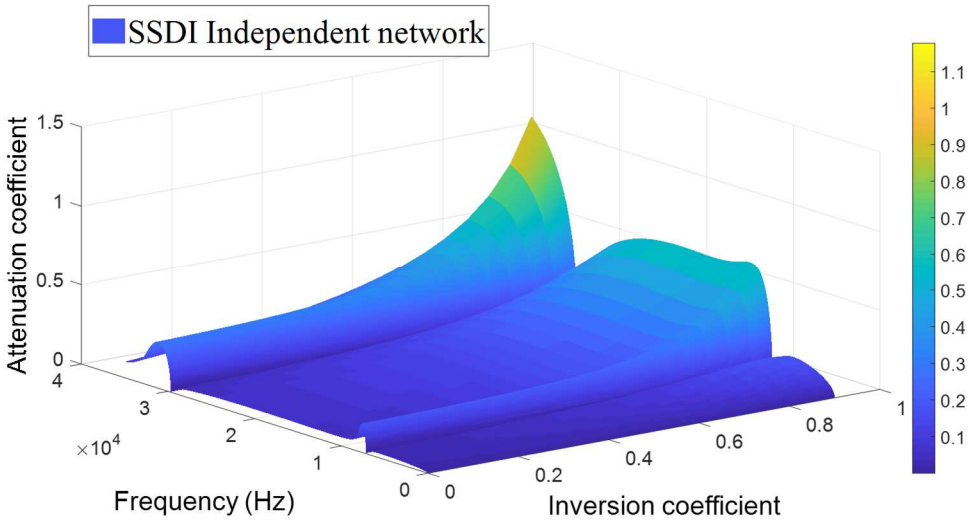
SSDI Independent network
Attenuation coefficient
Frequency (Hz)
Inversion coefficient

(a)

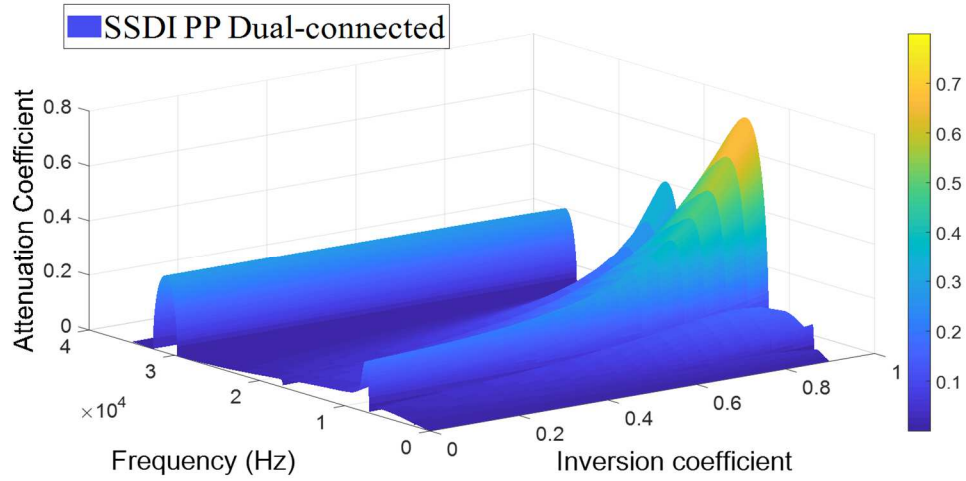
SSDI PP Dual-connected
Attenuation Coefficient
Frequency (Hz)
Inversion coefficient

(b)

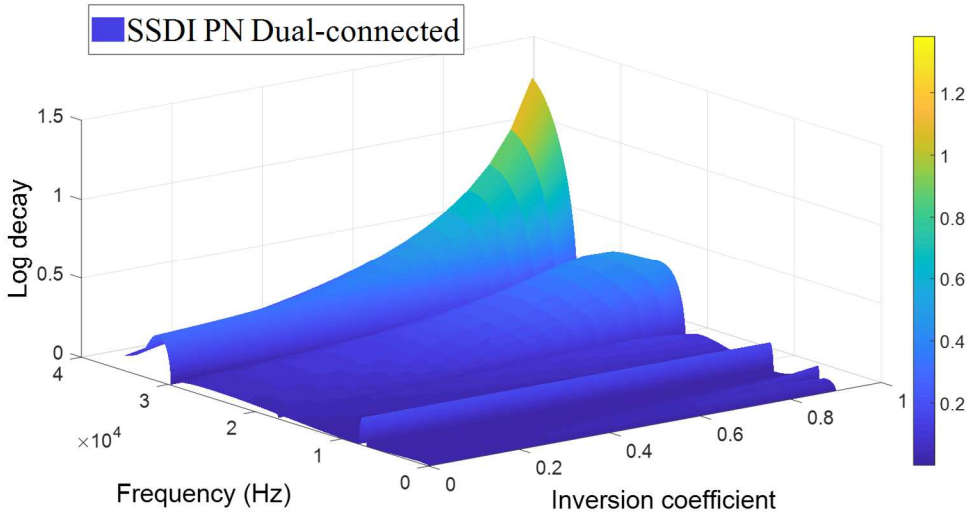
SSDI PN Dual-connected
Log decay
Frequency (Hz)
Inversion coefficient

(c)

Figure 11 3D plot of attenuation coefficient of propagative wave for (a) SSDI independent and (b) SSDI PP Dual-connected and (c) SSDI PN Dual-connected method versus voltage inversion coefficient ($\gamma_{diff} = \gamma^{\sqrt{\frac{1}{2}}}$).

In addition, in order to further demonstrate the damping performance and attenuation ability of the SSDI PP / PN Dual-connected approaches, transmission factors of propagative wave in finite beam metamaterial with different SSDI connection configurations under free-free boundary condition are calculated and compared. Herein, a finite piezoelectric beam composed of 8 minimal Bragg-type periodic cells arranged in a row along x direction is adopted as a sample for the performance assessment, as shown in Figure 12 (a). The investigated piezoelectric beam is 176mm long. Figure 12 (b) and Figure 12 (c) respectively show the piezoelectric beam sample with SSDI independent electrical networks and with SSDI PP / PN Dual-connected electrical networks. External force is applied to one side of the beam whose displacement amplitude is assumed to be equal to D_0, and the displacement amplitude of the other side of the beam is equal to D_8. Therefore, transmission factor K_{trans} of the finite beam metamaterial under various SSDI electrical boundary conditions can be obtained using the following equation:

$$K_{trans} = 20\log_{10}\left(\frac{D_8}{D_0}\right) \tag{19}$$

Figure 12 (d) shows the transmission factor of the beam sample with various electrical boundary conditions. Specifically, all the SSDI methods have good damping performance in the whole frequency range compared to open circuit condition. In the first two vibration modes, the SSDI PN Dual-connected method exhibits the best damping performance. From the 3rd mode to the 6th mode, the SSDI independent method shows the best damping performance. From the 7th mode to the 10th mode, the SSDI PP Dual-connected method has the best damping performance. Therefore, it can be seen that in some relatively broadband frequency ranges, the SSDI PP / PN Dual-connected methods can indeed be applied to improve the damping performance using less SSDI shunt branches than the SSDI independent approach as shown in Table 3, and can also be better adapted to low frequency (first vibration modes) control.

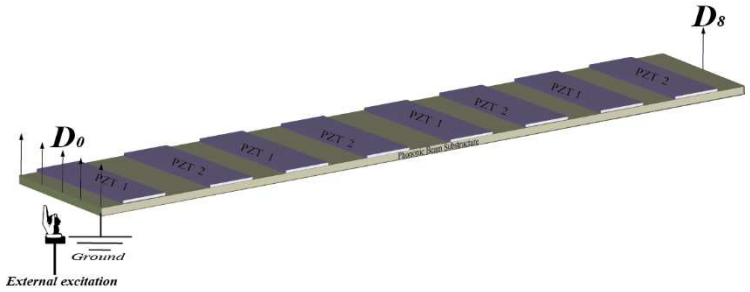

(a)

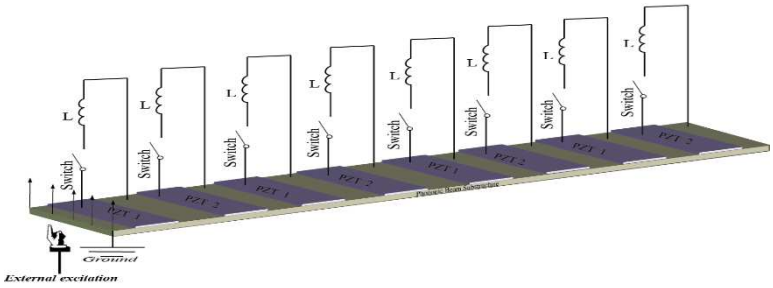

(b)

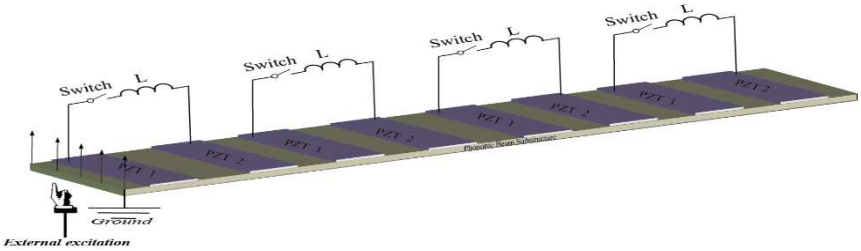

(c)

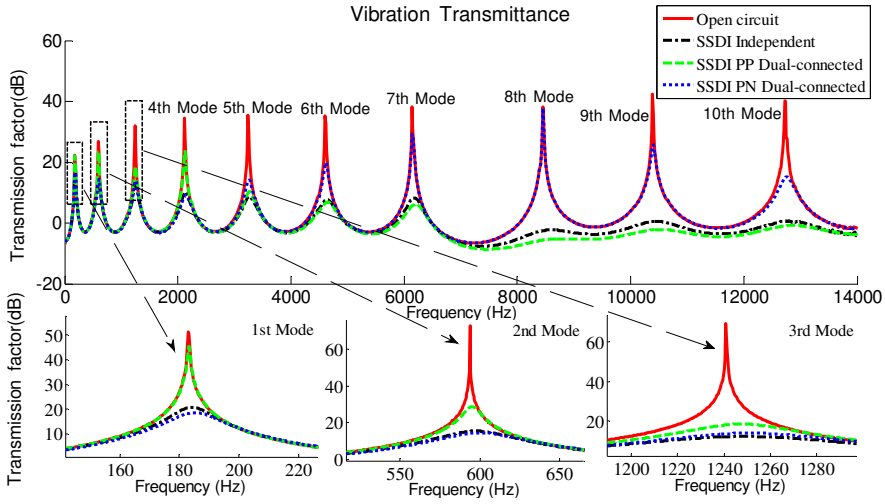

(d)

Figure 12 (a) Free-free piezoelectric phononic beam without electrical shunting networks and (b) with the SSDI independent networks and (c) with the proposed SSDI PP / PN Dual-connected networks and (d) transmission factor of the finite beam with different electrical boundary conditions. (γ=0.5, γ_{diff}=0.6).

Table 3 comparison of vibration transmittance performance and the number of SSDI shunts among different methods.

Methods	Vibration transmittance performance			Number of the SSDI shunts
	1^{st}-2^{nd} Modes	3^{rd}-6^{th} Modes	7^{th}-10^{th} Modes	
Open circuit	------	------	------	0
SSDI independent	------	Best	------	8
SSDI PP Dual-connected	------	------	Best	4
SSDI PN Dual-connected	Best	------	------	4

5. Experimental validation for the low frequency damping performance

In order to validate the low frequency damping performance and wave propagation control performance of the beam metamaterial featuring SSDI Dual-connected electrical networks, frequency responses of a clamped-clamped piezoelectric beam metamaterial using the different SSDI electrical networks are compared and discussed theoretically and experimentally in this section. The beam sample is composed of four Dual-connected periodic cells and the length of each Dual-connected cell is 44 mm. Parameters of the beam substructure and PZTs are those previously used and respectively listed in Table 1 and Table 2. The experimental setup is depicted in Figure 13. An external force, applied to the node between the 1^{st} and the 2^{nd} Dual-connected periodic cell, is generated by an electromagnet driven by an amplifier with the signal delivered by a function generator. The switching command for controlling the switching circuits is produced by a dSpace system for obtaining more precise experimental results. In practical applications, it is convenient to replace the dSpace system by integrated self-powered SSDI circuits as the switching control device [29]. An inductive displacement sensor is used for monitoring the displacement of the node between the 3^{rd} and the 4^{th} Dual-connected periodic cell. The steady state displacement is checked to remain sinusoidal for each measured point for ensuring the validity of the first harmonic approximation. Herein, only stationary waves can be considered since the steady state of flexural response is observed through the displacement of a single nodal point, which is consistent with the flexural nature of the vibration. Therefore, no phase delay for each considered mode appears. In order to better demonstrate the principle of SSDI PP/PN Dual-connected approaches on the periodic piezoelectric beam with finite length and certain boundary conditions and

consistent with the low frequency target, the first three resonant flexural vibration mode shapes of the investigated beam in the open circuit condition are calculated based on FE methods, as shown in Figure 14(a)-(c), respectively. Mode shape analysis demonstrates elastic wave propagation control and vibration control performance from the vibration damping aspect.

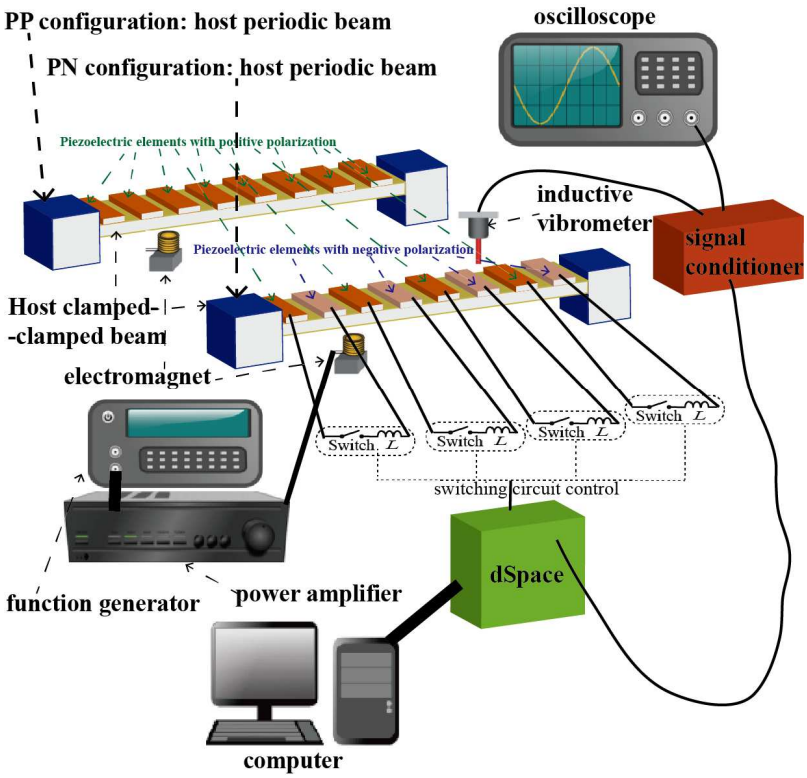

Figure 13 Experimental setup.

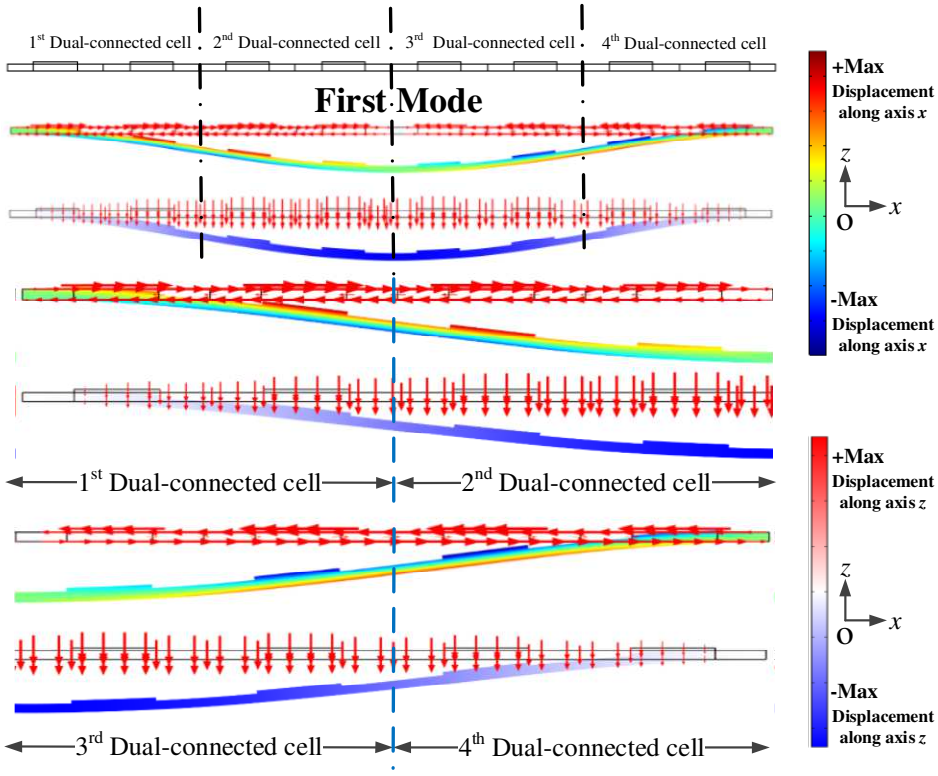
1st Dual-connected cell
2nd Dual-connected cell
3rd Dual-connected cell
4th Dual-connected cell
First Mode
+Max
Displacement
along axis x
z
x
O
-Max
Displacement
along axis x
+Max
Displacement
along axis z
-Max
Displacement
along axis z
1st Dual-connected cell
2nd Dual-connected cell
3rd Dual-connected cell
4th Dual-connected cell

(a)

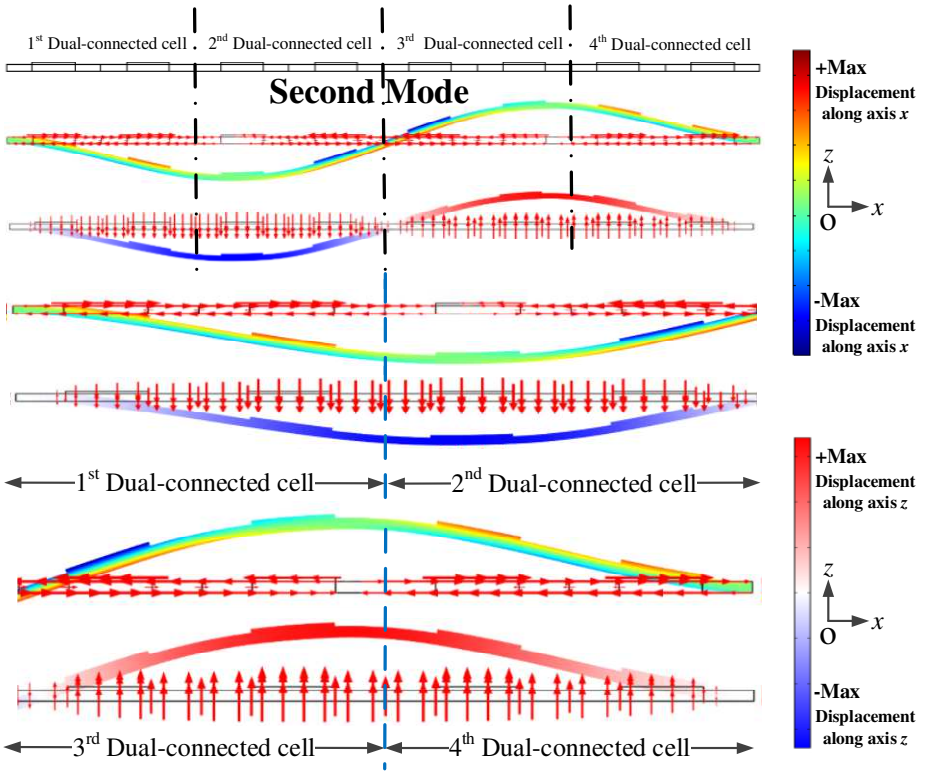
1st Dual-connected cell
2nd Dual-connected cell
3rd Dual-connected cell
4th Dual-connected cell
Second Mode
+Max
Displacement
along axis x
z
x
O
-Max
Displacement
along axis x
+Max
Displacement
along axis z
-Max
Displacement
along axis z
1st Dual-connected cell
2nd Dual-connected cell
3rd Dual-connected cell
4th Dual-connected cell

(b)

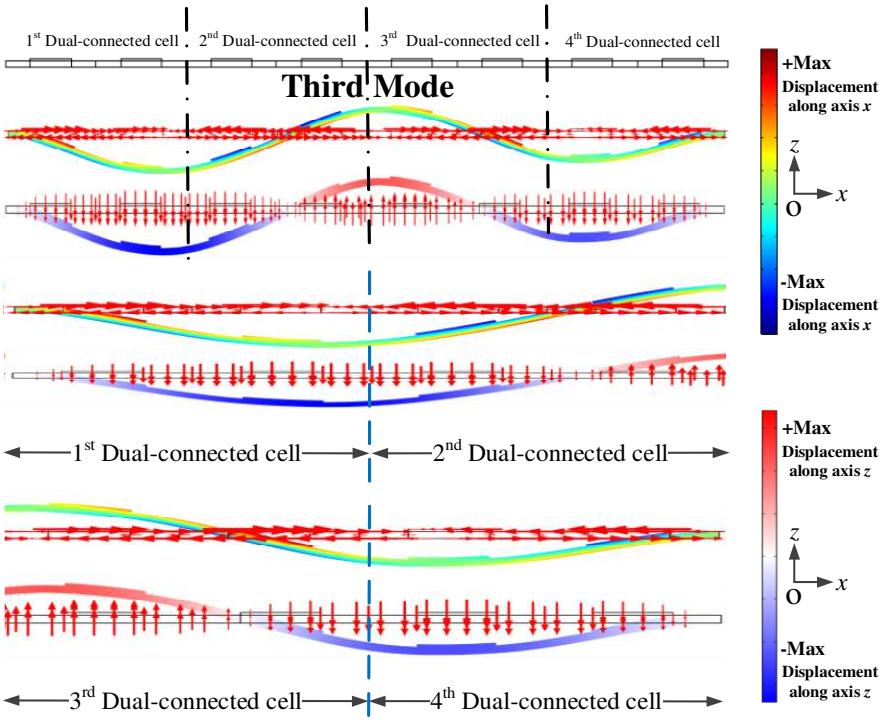

(c)

Figure 14 (a) First vibration mode shape, (b) second vibration mode shape and (c) third vibration mode shape of the clamped-clamped piezoelectric phononic beam at resonant frequencies in open circuit condition, and the corresponding flexural vibration displacement vector fields (the longitudinal strain along the axis x and the transverse strain along the axis z) represented by the color distribution and red arrows (displacement direction).

In order to reflect the experimental behavior and demonstrate the experimental results, structural damping is considered in the following theoretical analysis. Herein, Rayleigh damping, defining the damping matrix C_{unit} of one element as a function of mass and stiffness matrices of this single element (respectively noted M_{unit} and K_{unit}) as $C_{unit} = \beta_1 M_{unit} + \beta_2 K_{unit}$, is introduced in the frequency response analysis. According to preliminary experimental measurements, the coefficients β_1 and β_2 have been determined to be equal to $20\ s^{-1}$ and $13\times10^{-6} s$, respectively.

In experiments, the inversion coefficients in the SSDI independent and Dual-connected methods are equal to 0.5 and 0.6, respectively. Comparison of measured experimental displacement magnitudes and theoretical predictions in different methods is depicted in Figure 15(a) and (b), where the displacements have been normalized to the maximal displacement in open circuit conditions in each analysis (theoretical and experimental). Herein, it should be noted that although the inversion coefficients are set to moderate values for achieving better attenuation

performance, obvious excellent attenuation performance in different methods are not achieved since the structural damping of the used clamped-clamped piezoelectric beam is likely to be relatively high. However, the performance difference among different investigated methods can still be clearly found by comparison.

As shown in Figure 15, both of the theoretical and experimental results show that damping performance of the SSDI PN Dual-connected method is the best among all the methods for the first vibration mode, while the SSDI independent method has the best damping performance for the second mode and similar damping performance with the SSDI PP Dual-connected method for the third vibration mode, which is in good agreement with elastic wave attenuation performance of the investigated beam metamaterial as shown in Figure 8 and Figure 12 (d). Hence, SSDI 2-order Dual-connected method, especially in the PN configuration, is suitable for simple (only *4* switches are required versus *8* for the independent method) yet efficient low-frequency vibration control purposes.

In addition, frequency response results show that the SSDI PN Dual-connected approach achieves better damping performance than the SSDI PP Dual-connected approach in the first two vibration modes, and the SSDI PP Dual-connected method is better than the SSDI PN method in the third vibration mode, which can be explained by the principle of SSDI PP/PN Dual-connected approach. As shown in Figure 14(a), in the first vibration mode shape, two PZTs in each Dual-connected cell are all bended and compressed with the same strain direction, and thus the PN configuration can achieve higher voltage difference between two PZTs than the PP configuration, which causes that SSDI PN Dual-connected method exhibits better attenuation performance than SSDI PP Dual-connected method, as confirmed by theoretical and experimental frequency response results. As shown in Figure 14(b), in the second vibration mode shape, two PZTs in the 1st and the 2nd Dual-connected cells are bended and compressed with the same strain direction, and two PZTs in the 3rd and the 4th Dual-connected cells are bended and stretched with the same strain direction. Hence, similar to the first vibration mode, the SSDI PN Dual-connected method is better than the SSDI PP method in the second vibration mode demonstrated by theoretical and experimental frequency response results.

As shown in Figure 14(c), the 1st and 4th dual-connected cells, in which two PZTs are bended and compressed with the same strain direction, fit the PN connection, while the 2nd and 3rd dual-connected cells, in which two PZTs have the opposite strain direction (one PZT is bended and compressed, and the other one is bended and stretched), do not fit for the PN connection. Obviously, the converse observation stands for the PP Dual-connected method for this mode. Thus, there is a

counter-performance when using solely PP or PN methods. However, as shown in Figure 14(c), the 2nd and 3rd Dual-connected cells overall achieves larger longitudinal strain (along axis *x*) than the 1st and 4th Dual-connected cells, and thus may induce larger voltage difference. Due to such characteristics, PP effect is prevalent in the third mode. Therefore, the SSDI PP Dual-connected method is better than the SSDI PN Dual-connected method in the third vibration mode, which is also demonstrated by theoretical and experimental frequency response results. In addition, from these observations, it can be drawn that PP and PN Dual-connected cells can be mixed to provide better attenuation performance for a specific targeted vibration mode.

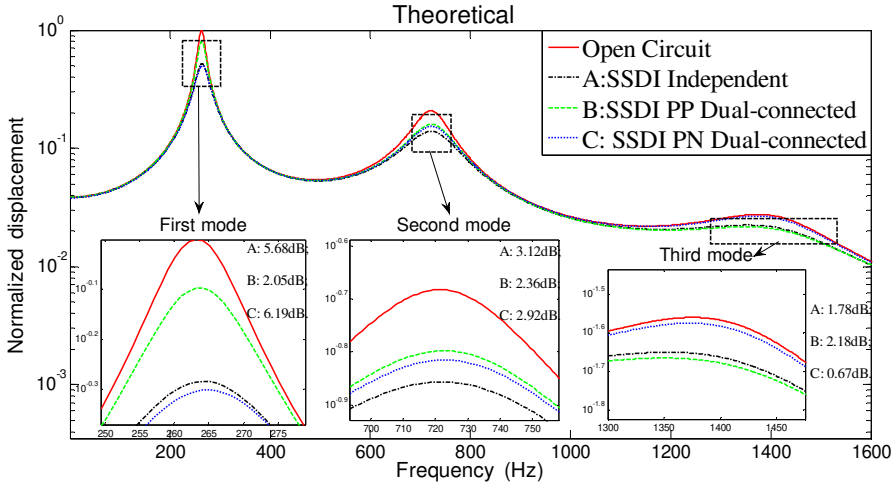

(a)

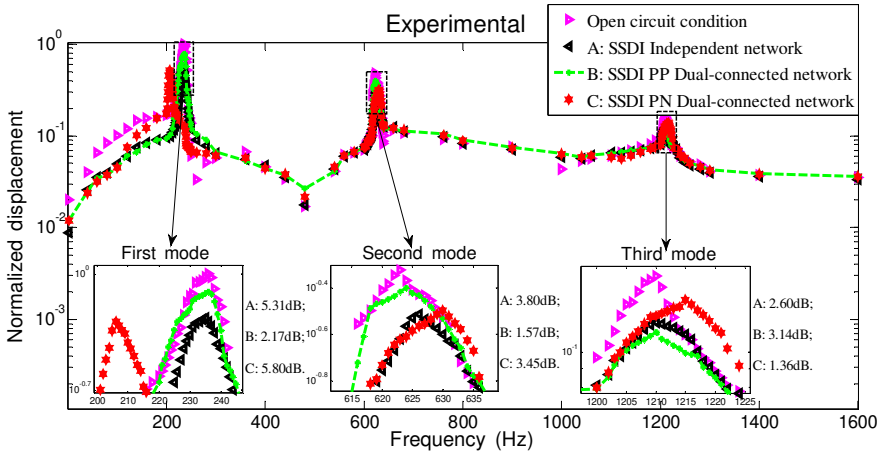

(b)

Figure 15 (a) Normalized theoretical displacement of the clamped-clamped piezoelectric phononic beam in different electrical boundary conditions; (b) normalized experimental displacement of the clamped-clamped piezoelectric phononic beam in different electrical boundary conditions.

6. Conclusion

Piezoelectric beam metamaterial with nonlinear SSDI Dual-connected networks is proposed in this article. The wave propagation properties are investigated theoretically based on finite element modeling method and wave propagation theory, and low-frequency damping performance is also demonstrated theoretically and experimentally. Results showed that wave attenuation performance of the proposed structure becomes worse with the increase of the order of the SSDI Dual-connected electrical networks. However, the proposed SSDI 2-order Dual-connected electrical networks for coupling the mechanical medium of the proposed structure can achieve better band gap hybridization (between broadly resonant-type stop band mechanism and Bragg-type stop band mechanism) than the SSDI independent electrical networks. Overall, the proposed metamaterial with SSDI PP Dual-connected electrical networks exhibits better band gap hybridization and thus attenuation performance near the first Bragg-type band gap, hence being more suitable for low-frequency vibration control. On the other hand, the proposed metamaterial with SSDI PN Dual-connected electrical networks shows better band gap hybridization performance near the second Bragg-type band gap, and better attenuation performance in the medium frequency region is achieved. In addition, the proposed structure with SSDI 2-order Dual-connected electrical networks has less SSDI shunts than the piezoelectric beam metamaterial with the SSDI independent electrical networks for achieving better wave attenuation performance in some specific frequency domains, hence providing simpler implementation and being less cumbersome.

Acknowledgments

The authors acknowledge the partial financial support from China Scholarship Council.
The authors declare no conflict of interest in preparing this article.

References

[1] Belle L V, Claeys C, Deckers E, et al., On the impact of damping on the dispersion curves of a locally resonant metamaterial: Modelling and experimental validation, J.Sound.Vib. 409 (2017) 1-23.

[2] Brillouin L, Wave Propagation in Periodic Structures: Electric Filters and Crystal Lattices, McGraw-Hill Book Company, Inc. New York, 4026 (1953) 926.

[3] Liu Z, Zhang X, Mao Y, Zhu Y Y, Yang Z, Chan C T and Sheng P, Locally resonant sonic materials, Science 289 (2000) 1734–1736.

[4] Lee J H, Singer J P, Thomas E L, Micro-/Nanostructured Mechanical Metamaterials, Adv. Mater. 24(36) (2012) 4782-4810.

[5] Neville R M, Scarpa F, Pirrera A, Shape morphing Kirigami mechanical metamaterials, Sci. Rep. 6 (2016) 31067.

[6] Goffaux C, Sánchez-Dehesa J, Yeyati A L, et al., Evidence of fano-like interference phenomena in locally resonant materials, Phys. Rev. Lett. 88(22) (2002) 225502.

[7] Wang G, Cheng J, Chen J, et al., Multi-resonant piezoelectric shunting induced by digital controllers for subwavelength elastic wave attenuation in smart metamaterial, Smart Mater. Struct. 26(2) (2016) 025031.

[8] Sugino C, Ruzzene M, Erturk A, Merging mechanical and electromechanical bandgaps in locally resonant metamaterials and metastructures, J.Mech.Phys.Solids. 116 (2018).

[9] Maldovan M, Sound and heat revolutions in phononics, Nature 503(7475) (2013) 209-217.

[10] Chang I L, Liang Z X, Kao H W, et al., The wave attenuation mechanism of the periodic local resonant metamaterial, J. Sound.Vib. 412 (2018) 349-359.

[11] Airoldi L and Ruzzene M, Design of tunable acoustic metamaterials through periodic arrays of resonant shunted piezos, New J. Phys. 13(11) (2011) 113010.

[12] Lu Y, Tang J, Electromechanical tailoring of structure with periodic piezoelectric circuitry, J. Sound.Vib. 331(14) (2012) 3371-3385.

[13] Ghazaryan K B, Piliposyan D G, Interfacial effects for shear waves in one dimensional periodic piezoelectric structure, J. Sound.Vib. 330(26) (2011) 6456-6466.

[14] Chen S, Wang G, Wen J, et al., Wave propagation and attenuation in plates with periodic arrays of shunted piezo-patches, J. Sound.Vib. 332(6) (2013) 1520-1532.

[15] Zhang H, Wen J, Xiao Y, et al., Sound transmission loss of metamaterial thin plates with periodic subwavelength arrays of shunted piezoelectric patches, J. Sound.Vib.343 (2015) 104-120.

[16] Nouh M A, Aldraihem O J, Baz A, Periodic metamaterial plates with smart tunable local resonators, J. Intell. Mater. Syst. Struct. 27(13) (2015)1829-1845.

[17] Bergamini A, Delpero T, De S L, et al., Phononic crystal with adaptive connectivity, Adv. Mater,26(9) (2014) 1343-1347.

[18] Maurini C, Dell'Isola F, Vescovo D D, Comparison of piezoelectronic networks acting as distributed vibration absorbers, Mech.Syst.Sig.Process 18(5) (2004) 1243-1271.

[19] Thorp O, Ruzzene M and Baz A, Attenuation and localization of wave propagation in rods with periodic shunted piezoelectric patches, Smart Mater. Struct. 10(5) (2001) 979-989.

[20] Bao B, Wang Q. Elastic wave manipulation in piezoelectric beam meta-structure using electronic negative capacitance dual-adjacent/staggered connections. Compos. Struct., 2019, 210: 567-580.

[21] Goffaux C, Sánchez-Dehesa J, Yeyati A L, et al., Evidence of fano-like interference phenomena in locally resonant materials, Phys. Rev. Lett. 88(22) (2002) 225502.

[22] Fan Y, Collet M, Ichchou M, et al., A wave-based design of semi-active piezoelectric composites for broadband vibration control, Smart Mater. Struct. 25(5) (2016) 055032.

[23] Zhou W, Chen W, Chen Z, et al. Actively controllable flexural wave band gaps in beam-type acoustic metamaterials with shunted piezoelectric patches. Eur. J. Mech-A/Solid, 2019: 103807.

[24] Tateo F, Collet M, Ouisse M, et al., Design variables for optimizing adaptive metacomposite made of shunted piezoelectric patches distribution, J. Vib. Control. (2014) 1077546314545100.

[25] Li Z N, Wang Y Z, Wang Y S, Nonreciprocal phenomenon innonlinear elastic wave metamaterials with continuous properties. Int. J. Solids. Struct. 150 (2018)125–134.

[26] Li Z N, Yuan B, Wang Y Z, et al., Diode behavior and nonreciprocal transmission in nonlinear elastic wave metamaterial. Mech.Mater. 133 (2019)85-101.

[27] Li Z N, Wang Y Z, Wang Y S., Tunable nonreciprocal transmissionin nonlinear elastic wave metamaterials by initial stress. Int. J. Solids. Struct. 182–183 (2020)218-235.

[28] Lallart M, Yan L, Richard C and Guyomar D, Damping of periodic bending structures featuring nonlinearly interfaced piezoelectric elements, J. Vib. Control. 22(18) (2015) 3930-3941.

[29] Lallart M, Lefeuvre E, Richard C and Guyomar D, Self-Powered Circuit for Broadband, Multimodal Piezoelectric Vibration Control, Sens. Act. A: Phys. 143(2) (2008) 277-382.

[30] Yan L-J, Bao B, Guyomar D and Lallart M, Periodic structure with interconnected nonlinear electrical networks, J. Intell. Mater. Syst. Struct. (2016) 1045389X16649448.

[31] Bao B, Guyomar D, Lallart M, Vibration reduction for smart periodic structures via periodic piezoelectric arrays with nonlinear interleaved-switched electronic networks, Mech. Syst. Sig. Process. 82 (2017) 230-259.

[32] Bao B, Guyomar D, Lallart M, Electron–phonon metamaterial featuring nonlinear tri-interleaved piezoelectric topologies and its application in low-frequency vibration control, Smart Mater. Struct. 25(9) (2016) 095010.

[33] Bao B, Guyomar D, Lallart M, Piezoelectric metacomposite structure carrying nonlinear multilevel interleaved-interconnected switched electronic networks, Compos. Struct. 161 (2017) 308-329.

[34] Wang Y Z, Li F M, Wang Y S., Active feedback control of elastic wave metamaterials. J. Intel. Mat. Syst. Str. 28(2017) 2110–2116.

[35] Bao B. Distributed, broadband vibration control devices using nonlinear approaches. Université de Lyon, 2016.

Appendix: A brief Finite element modelling of Euler-Bernoulli piezoelectric beam

Under the Euler-Bernoulli assumptions, assumptions of the stress/strain components are made:

$$\begin{cases} T_3^p = T_4^p = T_5^p = T_6^p = 0 \\ S_2^p = S_3^p = S_4^p = S_5^p = S_6^p = 0 \end{cases} \tag{20}$$

And thus the constitutive piezoelectric equations can be further reduced as:

$$\begin{bmatrix} S_1^p \\ S_2^p \\ D_3 \end{bmatrix} = \begin{bmatrix} s_{11}^E & s_{12}^E & \sigma d_{31} \\ s_{21}^E & s_{22}^E & \sigma d_{31} \\ \sigma d_{31} & \sigma d_{31} & \varepsilon_{33}^T \end{bmatrix} \begin{bmatrix} T_1^p \\ T_2^p \\ E_3 \end{bmatrix} \tag{21}$$

where σ is the sign of the piezoelectric constant which depends on the polarization of the piezoelectric material.

Then, the longitudinal stress of the PZT patch can be given as:

$$T_1^p = \frac{s_{11}^E}{\left(s_{11}^E\right)^2 - \left(s_{12}^E\right)^2} S_1^p - \frac{\sigma d_{31}}{s_{11}^E + s_{12}^E} E_3 \tag{22}$$

The electrical field is expressed as a function of the piezoelectric voltage V_p:

$$E_3 = -\frac{V_p}{t_p} \tag{23}$$

Where t_p is the thickness of the PZT patch.

Therefore, the stress T_1^p of Eq.(22) can be further rewritten as:

$$T_1^p = E_p S_1^p + \frac{\sigma d_{31}}{t_p\left(s_{11}^E + s_{12}^E\right)} V_p, E_p = \frac{s_{11}^E}{\left(s_{11}^E\right)^2 - \left(s_{12}^E\right)^2} \tag{24}$$

where E_p denotes elastic rigidity of the PZT patch in-plane strain.

Normally, the longitudinal strain is defined as the distance from the second spatial derivative of the deflection u_3 and the neutral axis x_c. Based on the Euler-Bernoulli beam theory, the strain along axis *x* has the following form:

$$S_1 = -\left(z - x_c\right)\frac{\partial^2 u_3}{\partial x^2} \tag{25}$$

Assuming that $z = 0$ is the lower surface of the beam, the neutral axis x_c of the beam element without PZT patches can be given by:

$$x_c = \frac{t_b}{2} \tag{26}$$

where t_b is the thickness of the pure beam without PZT patches.

The neutral axes of different beam elements can also be written as:

$$x_c = \frac{E_b t_b^2 + E_p t_p^2 + 2 t_b t_p E_p}{2\left(E_b t_b + E_p t_p\right)}, \text{ PZT patches cover one surface} \tag{27}$$

where E_b denotes the elastic modulus of the pure beam without PZT patches - $E_b = \frac{Y_b}{1-\left(v_b\right)^2}$: Y_b and v_b respectively refer to the Young modulus and Poisson's ratio of the pure beam substructure.

Thus,

$$\begin{cases} T_1^b = -(z - x_c)\dfrac{\partial^2 u_3}{\partial x^2} E_b \\ T_1^p = -(z - x_c)\dfrac{\partial^2 u_3}{\partial x^2} E_p + \dfrac{\sigma d_{31}}{t_p\left(s_{11}^E + s_{12}^E\right)} V_p \end{cases} \tag{28}$$

where T_1^b denotes the stress of the pure beam structure along *x*-axis.

Therefore, the bending moment of the piezoelectric beam $M_{bending}^{Euler-B}$ can be given as:

$$M_{bending}^{Euler-B} = w_b \int T_1 (z - x_c)\, dz = \begin{cases} E_b I_b \dfrac{\partial^2 u_3}{\partial x^2}, T_1 = T_1^b \\ E_{eq} I_{eq} \dfrac{\partial^2 u_3}{\partial x^2} + b_1 V_p, T_1 = T_1^b + T_1^p \end{cases} \tag{29}$$

Where w_b is the width of the pure beam (the PZT patch is assumed to have the same width as the pure beam structure), T_1 is the strain of the piezoelectric beam along *x*-axis. $E_{eq} I_{eq} = E_b I_b + E_p I_p$ (I_b and I_p are respectively the second moment of area of the pure beam structure's cross-section and the second moment of area of the piezoelectric element's cross-section), and $b_1 = -\dfrac{\sigma d_{31} w_b}{t_p\left(s_{11}^E + s_{12}^E\right)} \int_{t_b}^{t_b + t_p} (z - x_c) dz$.

1. Dynamical equations of the piezoelectric beam in the mechanical domain

The elastic waves in the piezoelectric beam are governed by the following differential equations:

$$\rho A_c \frac{\partial^2 u(x,t)}{\partial t^2} + EI_s \frac{\partial^2 M_{bending}^{Euler-B}}{\partial x^2} = q(x,t) \tag{30}$$

Thus, the mechanical equations of unit FE beam element can be given with Hermitian shape functions *H*(*x*) as:

$$\begin{cases} [M_{cell}]\{\ddot{d}^{ni}\} + [K_{cell}]\{d^{ni}\} = \{F^{ni}(t)\}, & \text{beam element without PZTs} \\ [M_{cell}]\{\ddot{d}^{ni}\} + [K_{cell}]\{d^{ni}\} + [B_1^{N-order}]\{V_p^{ni}\} = \{F^{ni}(t)\}, & \text{beam element with PZTs} \end{cases} \tag{31}$$

$$\begin{cases} [M_{cell}]=\int_0^l [H]^T \rho A_c [H]dx, \quad [K_{cell}]=\int_0^l [H'']^T EI_s [H'']dx, \quad \left[F^{ni}(t)\right]=\int_0^l q(x,t)[H]^T dx \\ \left[B_1^{N-order}\right]=\int_0^l b_1 [H'']^T dx, \end{cases}$$

$$\rho A_c = \begin{cases} \rho_b A_b, & \text{beam element without PZTs} \\ \rho_b A_b + \rho_p A_p, & \text{beam element with PZTs} \end{cases}$$

$$EI_s = \begin{cases} E_b I_b, & \text{beam element without PZTs} \\ E_{eq} I_{eq}, & \text{beam element with PZTs} \end{cases}$$

A damping matrix should also be added in the mechanical equations to relate losses in experimental structures, which can be for example modeled as Rayleigh damping, yielding:

$$\begin{cases} [M_{cell}]\{\ddot{d}^{ni}\}+[C_{cell}]\{\dot{d}^{ni}\}+[K_{cell}]\{d^{ni}\}=\{F^{ni}(t)\}, & \text{beam element without PZTs} \\ [M_{cell}]\{\ddot{d}^{e}\}+[C_{cell}]\{\dot{d}^{ni}\}+[K_{cell}]\{d^{ni}\}+\left[B_1^{N-order}\right]\{V_p\}=\{F^{ni}(t)\}, & \text{beam element with PZTs} \\ [C_{cell}]=\beta_1[M_{cell}]+\beta_2[M_{cell}], \beta_1 \text{ and } \beta_2 \text{ are constant coefficients} \end{cases} \quad (32)$$

And thus, the mechanical equations of unit FE beam element in the frequency domain can be given as:

$$\begin{cases} \left[-\omega^2 M_{cell}\right]\{d^{ni}\}+[j\omega C_{cell}]\{d^{ni}\}+[K_{cell}]\{d^{ni}\}=\{P^{ni}\}, & \text{beam element without PZTs} \\ \left[-\omega^2 M_{cell}\right]\{d^{ni}\}+[j\omega C_{cell}]\{d^{ni}\}+[K_{cell}]\{d^{ni}\}+\left[B_1^{N-order}\right]\{V_p\}=\{P^{ni}\}, & \text{beam element with PZTs} \\ [C_{cell}]=\beta_1[M_{cell}]+\beta_2[M_{cell}], \beta_1 \text{ and } \beta_2 \text{ are constant coefficients} \end{cases} \quad (33)$$

2. Dynamical equations of the piezoelectric beam in the electrical domain

The electrical relationships between the electrical displacement and the piezoelectric voltage can be summarized as:

$$D_3 = \frac{-\sigma d_{31} t_p}{\left(s_{11}^E + s_{12}^E\right)} \frac{\partial^2 u_3}{\partial x^2} + \frac{2\left(d_{31}\right)^2 - \varepsilon_{33}^T \left(s_{11}^E + s_{12}^E\right)}{t_p \left(s_{11}^E + s_{12}^E\right)} V_p \quad (34)$$

Then, by integrating the electrical displacement over the length L_p of the PZT patch, the electric charge quantity Q of one PZT patch can be given in matrix-vector notation:

$$\{Q\} = \left[B_2^{N-order} \right] \{d^{ni}\} + \left[B_3^{N-order} \right] \{V_p\} \tag{35}$$

$$\left[B_2^{N-\text{order}} \right] = \frac{-[\sigma] w_b d_{31} t_p}{\left(s_{11}^E + s_{12}^E \right)} \int_0^l [H''] dx$$

$$\left[B_3^{N-\text{order}} \right] = \frac{w_b \left[2 d_{31}{}^2 - \varepsilon_{33}^T \left(s_{11}^E + s_{12}^E \right) \right]}{t_p \left(s_{11}^E + s_{12}^E \right)} \left[L_p \right]$$

And thus, the output currents I_p of one piezoelectric element can be given as:

$$\{I_p\} = \left[j\omega B_2^{N-order} \right] \{d^{ni}\} + \left[j\omega B_3^{N-order} \right] \{V_p\} \tag{36}$$

where $[\sigma]$ and $\left[L_p \right]$ denote diagonal matrices which respectively depend on the sign of polarization direction of the bonded PZT patches and the length of the bonded PZT patches.

Thus, the electro-elastic relationships of FE modeling of the periodic piezoelectric beam based on the Euler-Bernoulli beam theory can be summarized as:

$$\begin{cases} \left[-\omega^2 M_{cell} \right] \{d^{ni}\} + [j\omega C_{cell}] \{d^{ni}\} + [K_{cell}] \{d^{ni}\} + \left[B_1^{N-order} \right] \{V_p\} = \{P^{ni}\} \\ \{I_p\} = \left[j\omega B_2^{N-order} \right] \{d^{ni}\} + \left[j\omega B_3^{N-order} \right] \{V_p\} \end{cases} \tag{37}$$

More detailed FE modeling methodologies for piezoelectric metamaterials with electrical networks can be found in Chapter 2 of the dissertation [35].